



---

# Nebular Chewing Gum: A Modeled Radiation Field Search for Bubble Structures in the Greater Orion Nebula Region

---

FIRST-YEAR PROJECT  
submitted in partial fulfillment of the  
requirements for the degree of

MASTER OF SCIENCE  
in  
ASTRONOMY

Author :  
Student ID :  
Supervisor :

Catherine Slaughter  
S3238865  
Dr. Alexander Tielens

Leiden, The Netherlands, July 31, 2022

# Nebular Chewing Gum: A Modeled Radiation Field Search for Bubble Structures in the Greater Orion Nebula Region

Catherine Slaughter

Huygens-Kamerlingh Onnes Laboratory, Leiden University  
P.O. Box 9500, 2300 RA Leiden, The Netherlands

July 31, 2022

## Abstract

*Context.* In order to better understand the way the universe changes with time, it is crucial to deeply understand stellar feedback. The Orion Molecular Cloud is the closest star-forming region to Earth, and has been studied extensively in order to better our understanding of how stars interact with their environment. Expanding these studies into new regions would be immensely useful to enhance our understanding, and new methods for finding such regions would be helpful to this end. Particularly massive O and B type stars are especially energetic, and therefore especially important for understanding stellar feedback.

*Aims.* We aim to establish and test a new method for searching for regions with particularly interesting stellar feedback in nebulae. We use the Greater Orion Nebula region for this test, as it is so well understood.

*Methods.* Using scoby, a code created to model radiation field strength in star clusters, we are able to compare the modeled radiation field from the O and B type stars in the area both with and without the influence of  $\theta^1$  Ori C. In doing so, we identify several regions where we can expect local feedback to be dominated by stars that are not  $\theta^1$  Ori C. We use velocity spectrum averaging and PV diagram analysis to search for bubble structures in these areas.

*Results.* We easily find the usual (M42, M43, NGC 1977) regions of interest in this area with our radiation-field method, as well as several others that have not

previously been studied. Our analysis of velocity structures near  $\theta^2$  Ori A and HD 37150 indicate bubbles around these stars.

*Conclusions.* We find that our modeled radiation field region-finding method is an effective way to search for possibly unknown regions of interest in the study of stellar feedback, especially in nebulae with a single (or few) dominant star(s). We also strengthen previous studies of possible bubble structure around  $\theta^2$  Ori A, and introduce a possible bubble structure near HD 37150

Chapter **1**

# Introduction

Bubble structures are pervasive in the ISM (Churchwell et al., 2006). The largest of which are created by supernovae and other transient, high-energy events. More recent studies, however, focus on smaller bubbles that form over time. Either by the blowing of stellar winds (Pabst et al. (2019), Pabst et al. (2020), Tiwari et al. (2021), Luisi et al. (2021)), or, more commonly, through a large drop off in radiation pressure in the nearby HII region, sometimes referred to as a “Spitzer” expansion (Pabst et al. (2020)). In some cases, both mechanisms may be at play (Bonne et al. (2022)). These bubbles are useful to help us better understand the role of stellar feedback in the structure of the ISM, and star formation rates (Walch et al. (2013))—both of which are the basis of much of our understanding of larger-scale structure in the galaxy. As a result, it is incredibly useful for us to be able to easily identify regions of high or otherwise unexpected stellar feedback. Often, especially in areas where the ISM is particularly clumpy or uneven in structure, these feedback bubbles form unevenly.

The greater Orion Nebula region (sometimes colloquially referred to as “Orion’s Sword”) is one such area. This region of the constellation Orion consisting of well-known gas structures such as M42 (the Orion Nebula), NGC 1977, and M43. It sits centered in Barnard’s Loop (an old supernova remnant) between and slightly to the right of the Orion A and Orion B molecular clouds, in the southern part of the Orion Molecular Cloud Complex. This region is the closest star-forming region to Earth, and, as a result, has been the subject of astronomical research related to star formation and feedback for many years, going as far back as Christiaan Huygens’ work in 1659.

Because of this region’s proximity to Earth, it is easy to observe, and in recent years has been observed using a variety of instruments and in a variety of wavelengths of light. We have extensive knowledge of its structure. In particular, we have come to know a great amount about the bubble structures in NGC

1977, M43, and M42, particularly the Veil surrounding the Huygens region and the Trapezium cluster (Güdel et al. (2008), van der Werf et al. (2013), Goicoechea et al. (2015), Abel et al. (2019), Pabst et al. (2019), Goicoechea et al. (2020), Pabst et al. (2020)).

For our purposes, the proximity of and wealth of knowledge about this region make it useful for testing out a new method for searching for regions of enhanced stellar feedback from relatively weak O and B type stars. While recent papers (Kavak et al. (2022a)) start with known velocity structures and search for regions that are interesting in their radiative output, we aim to do the opposite. We search for regions of relative radiative interest, and search for velocity structures there. It is commonly assumed that the majority of the radiation field in this region is dominated by  $\theta^1$  Ori C, an O7 class star and the brightest of the trapezium (Pabst et al., 2019). We are searching for regions where this assumption might break down, and looking for new bubble structures in these regions of interest.

Chapter **2**

# Observational data

## 2.1 O and B Star Data

The full data set of stars used in this study was pulled together by querying SIMBAD in the region covered by the SOFIA CII data (section 2.2) for all stars with 'O' or 'B' in their spectral classification. The region queried stretches (in decimal degrees) in right ascension from  $-5.9339^{\circ}$  to  $-4.4539^{\circ}$  and in declination from  $83.1833^{\circ}$  to  $84.3042^{\circ}$ . The resulting data set included 43 stars. One of these stars was removed manually, as its spectral type string ("A3IVeb") was accidentally caught by the filter. For most of the data set, the coordinate and parallax data came from Gaia EDR3 (Gaia Collaboration, 2020), for one star (HD 36865) these data comes from DR2 (Gaia Collaboration, 2018), and for two others, they come from Hipparcos (van Leeuwen, 2007). The spectral type data comes from a variety of sources (Sota et al., 2011; Nesterov et al., 1995; Hillenbrand, 1997; Houk & Swift, 1999; Levenhagen & Lester, 2006; Mason et al., 1998; Warren & Hesser, 1977; Burssens et al., 2020; Herbig, 1950; Abt, 2008). The full set of stellar data used, and the sources of each can be found in Table A.1 in Appendix A.

From here, stars without a parallax in SIMBAD were removed. Because this region is so nearby, and its extinction so well understood, we can safely assume that any star that does not have at least a Gaia DR2 parallax is either too far away to be solidly within the association, or too dim to be concerned with in the context of this study. An additional Parallax filter was applied based on the process used in Zari et al. (2017), and with additional consultation from Dr. Anthony Brown at Leiden University. Allowing for a relatively high range, only those stars with Parallax between The Parallax filtering steps brought the data set down to 37 stars.

To finalize the data set, the spectral class strings of two stars where manually

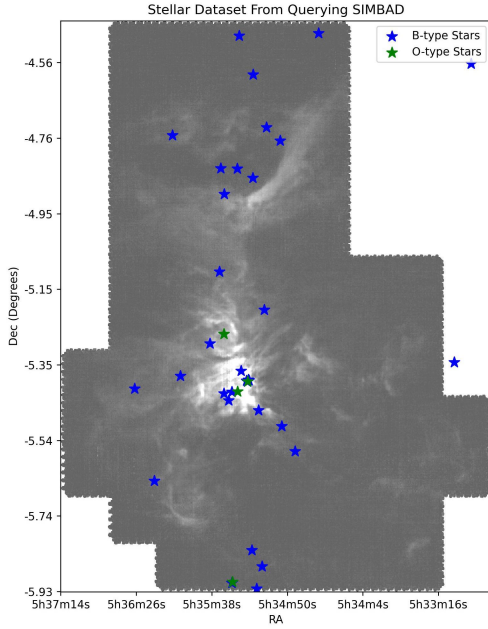


Figure 2.1 The final stellar data set, overlaid on a CII data image of the region for reference. B-type stars are shown in blue, while O-type stars are shown in green.

altered in preparation for use in the radiation field modeling code. The first, 42 Orionis (sometimes called c Orionis) is the primary illuminating star for NGC 1977. 42 Orionis is a tightly-bound binary star system, wherein the primary has a spectral type of B1V, and its companion is of unknown spectral type. As such, its SIMBAD spectral type string is 'BIV+?', which cannot be parsed by the radiation field code. We hard-code its spectral type string to 'B1V'. This was deemed justifiable as we are only concerned with O and B-type stars. If the companion star is too dim for us to observe its spectral class, it is almost certainly not an O or B-type star, so we are not concerned with it.

The second, HD 37150, is a B3III/IV-type star in the south eastern part of the region. Because of the regular expressions used to parse spectral type strings, and way the radiation field code accounts for uncertainty (subsection 3.1.1) in spectral types, this star was, at first being modeled as either a B3III or a B3I star. The difference in expected radiative output from a luminosity class III (ordinary giant) star to a luminosity class IV (subgiant) star is significantly less than the difference between a class III and class I (supergiant) star. Beyond the fact that HD 37150 is simply not a class I star, this increased possible difference in spectral class can create nonphysical results when comparing several modeled

radiation field maps.

Upon consultation with the code's author, we determined the best course of action was to hard-code the star as luminosity class III. The way the code handles luminosity classes (see section 3.1), this is essentially what is being done under the hood anyway. Ultimately, the specific luminosity class of the star that we input only changes the modeled radiation field maps. These maps are used primarily as a means of identifying regions of interest in the area, and the region around HD 37150 shows up as a region of interest regardless of if the luminosity class is hard-coded in as III or IV.

## 2.2 SOFIA UpGREAT CII Map

The first large data set used is the CII-transition map presented by Pabst et al. (2019) (and Pabst et al. (2020)) and is shown in Figure 2.2. This map was taken with the upGREAT (German Receiver for Astronomy at Terahertz Frequencies) heterodyne receiver on the SOFIA aircraft (Risacher et al. (2016)). The SOFIA aircraft is an airborne observatory built from a modified Boeing 747. It allows for observations to be made from high up ( $\sim 13\text{km}$ ), giving observers the opportunity to view frequencies normally absorbed by the atmosphere.

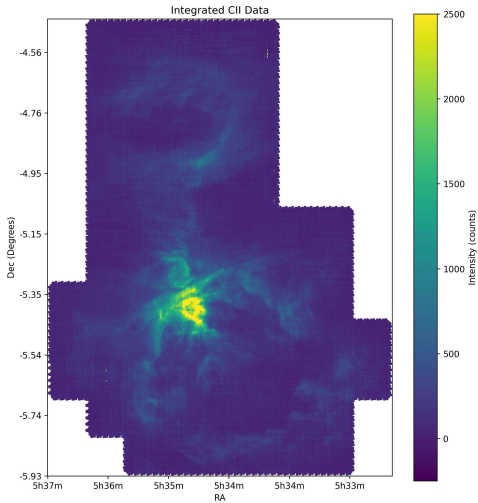


Figure 2.2 The CII data from Pabst et al. (2019), integrated over radial velocities with reasonable signal ( $v_{LSR} \approx -9.5$  to  $v_{LSR} \approx 14$ ).

The whole map covers a 1.2 square-degree-sized area of the sky with 16 arcsec of angular resolution. Each pixel of the map has an associated radial veloc-

ity spectrum. The raw data cube contains observations with for radial velocity ranging from -100 to 100 km/s, with a resolution of 0.3km/s. This, of course, is somewhat “overkill” and in reality, many of these frames contain very little signal. We cut down the data cube to 85 frames where the signal was clearly distinct from the noise. In the final cube we used, the radial velocity ranges from -9.19 km/s to 16 km/s.

## 2.3 Herschel 70 and 160 $\mu\text{m}$ Maps

To get a sense of the expected temperature in the regions, we use the 70 and 160  $\mu\text{m}$  maps from Herschel PACS (Poglitsch et al. (2010)), shown in Figure 2.3. Herschel is a space telescope with a 3.5-m primary, and observes in infrared to submillimeter wavelengths. These maps, first taken as a part of the GT2\_pandre observing program, have a pixel scale of  $8.88 \times 10^{-4}\text{°}$  and cover a region of the sky ranging from  $\sim -7^{\circ}22'$  to  $\sim -2^{\circ}58'$  in declination and  $\sim 5\text{hr}26\text{min}$  to  $\sim 5\text{hr}43\text{min}$  in right ascension.

In order to use these data as a proxy for dust temperature, we divide the 70micron map by the 160micron map. Additionally, for our purposes, we only need to see the greater Orion Nebula region, so we crop our temperature map to approximately the same area covered by the CII data. This leaves us with a 1200 by 1700-pixel map, or about 0.96 by 1.36 degrees.

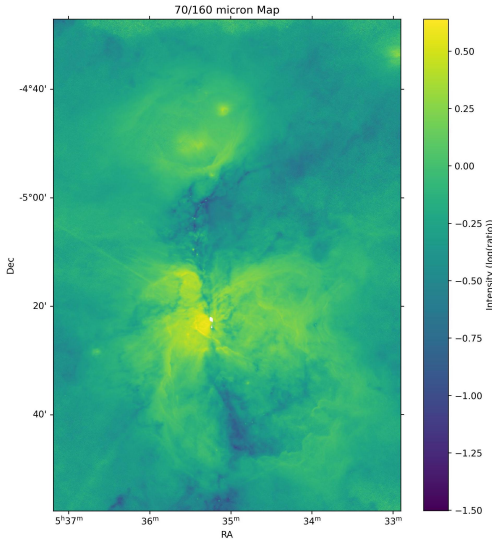


Figure 2.3 The temperature map created from the 160 and 70 $\mu\text{m}$  Herschel data, cropped to showcase the Orion Nebula region

# Chapter 3

## Methods

While previous studies of this region have focused on searching for areas with different ionization sources based on mechanical structures (particularly velocity), we take the opposite approach. By looking for regions where we expect alternative sources of ionization, we can pinpoint where we expect to see various velocity structures. We do so by creating a data set of O and B stars in the region, and modeling the expected radiation field strength from said set. From there, we can pick out regions of interest based on modeled radiation field strength, and analyze their velocity structures.

### 3.1 Creation of $G_0$ Radiation Field Maps

In order to model the expected impact of radiation from stars in this region, we make use of Spectra from Catalogs of OB stars (“scoby”)\*. This code, written primarily by Ramsey Karim at the University of Maryland, works for our purposes by taking in a Pandas Dataframe of stars (with spectral type strings and SkyCoord objects of their RA and dec positions) and an image world coordinate system (WCS) to create a map of the same size, shape, and resolution as the WCS showing the combined radiation field of the stars in Habing units ( $G_0$ ). Scoby works similarly to the cluster property synthesis done in the Starburst99 (Leitherer et al. (1999)) code. In contrast, however, scoby uses an observed catalog as opposed to a synthesized distribution of stars.

This code makes use of POWR model grids (Hamann & Gräfener (2004); Todt et al. (2015); Sander et al. (2012); Hainich et al. (2019)), and a number of luminosity class calibration tables outlined in Martins et al. (2005). It should be noted that these calibration tables only specifically account for types I, III, and

---

\*<https://github.com/ramseykarim/scoby>

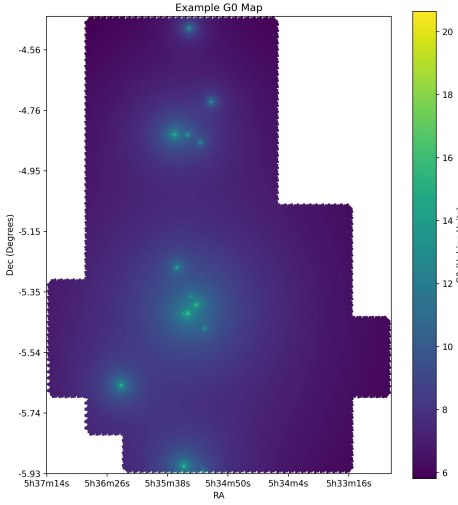


Figure 3.1 An example radiation field map, created with the entire stellar data set.

V. As a result, stars of “in-between” classes are assigned to one of these three in the scoby code. This is why it is acceptable to hard-code in the luminosity class of HD 37150 as a type III for our modeling purposes, as the code would do so under the hood anyway, even if the spectral class string were to be parsed correctly.

A further description of the methodology used by scoby can be found in Tiwari et al. (2021), though the code had not been brought into an isolated package for this paper, and, as such, is not yet referred to as “scoby.”

### 3.1.1 Randomness in the scoby code

In order to account for uncertainty in stellar spectral type, the scoby code automatically includes a bit of randomness in order to generate error values. For stars of a “known” spectral type, say, a star put into SIMBAD as an O5, the modeled spectral type has a small, but nonzero chance of being a half type different. So, for the example O5 star, it is assumed to be either an O4.5, O5, or O5.5 star (with O5 being weighted higher) when randomly sampled. In the case of stars of an “unknown” spectral type, like one listed as an O5/6 star, both options are taken into consideration and sampled in the same way. The code randomly samples every star to make a “realization” of the cluster, and calculates the re-

sulting radiation field. This is done many, many times, and the median value of all the radiation fields is output to the user.

This understanding has two significant impacts on this report. The first is that the code outputs error values along with the median radiation field map. Secondly, the way scoby handles randomness means that, when doing a pixel-to-pixel comparison of maps, the results can sometimes change from run to run. For our purposes, however, we are only using the scoby radiation fields as a way of identifying general regions of interest (section 3.2) for analyzing the CII and Herschel data. As a result, we largely do not make use of the error values except in Figure 4.6 and Figure 4.9 (the error bars are ultimately too small to see). Additionally, small deviations in the pixel values from run to run were found to not change our overall results.

## 3.2 Region-of-Interest Finding with Radiation Field Map Comparison

While it is generally assumed that the majority of radiation in the OMC1 region comes from  $\theta^1$  Ori C, we are interested in searching for regions where the local radiation field is dominated by other stars. We can use the scoby code to do this by making two maps. The first is a model of the radiation field of the region using *all* the stars listed in Table A.1. The second is a similar map, but with  $\theta^1$  Ori C removed from the input dataset. This shows us what the radiation field of the region would look like without  $\theta^1$  Ori C's influence without making any further assumptions as to the formation history of such a theoretical cluster.

By taking the ratio (Figure 4.1) of the latter over the former map, we can identify areas where the radiation from non- $\theta^1$  Ori C stars dominates. We more clearly see these regions by creating a mask of the whole map, and highlighting only those pixels where the ratio exceeds a chosen cutoff value (Figure 4.2). These become our regions of interest for study, and we can analyze our CII and temperature data in just these regions. Additionally, we can assess how our CII and temperature data may differ within regions of interest, compared to outside of them.

Upon assessing the appearance of the region mask at various cutoff values (Figure 4.2), we decide to use a cutoff of .95 for our study. This means that our regions of interest are ones where, according to the scoby maps, we expect the radiation from non- $\theta^1$  Ori C stars to make up about 95% of the total radiation in the region. It is important to note that the scoby code does not take in any data related to the gas structure of the region, so structures like PDRs can change how the radiation field look in reality. That being said, again, we only use the

radiation field models to search for regions that may warrant further research, so this is largely unimportant to our results.

### 3.3 Whole-Field Trend Assessment

Once we have created our region mask for the whole area, we begin by doing a general assessment of all regions of interest in aggregate. We begin by integrating over the radial velocity axis in our CII data cube. This is done by looking through the cube in DS9, and determining the minimum and maximum values where there is a significant enough signal that it can be found above the image noise. Then, the frames are added together. The Herschel data used to calculate a proxy for gas temperature is already a single frame, so a similar step is not necessary. From here, we can create histograms of the data points for each data map (Figure 4.8 and Figure 4.10). In doing so, we look to see if there is any difference in the distribution of values in vs. outside of the regions of interest. Next, we look at general trends in CII (Figure 4.6) and gas temperature (Figure 4.9) values vs. the expected radiation field for all the points both inside and outside the regions of interest according to our mask. Of course, each of these maps has over a million pixels, so the goal here is simply to look for general trends in data, and features that may be unique.

### 3.4 Velocity Structure Assessment

In order to search for interesting structures and bubbles in our regions of interest, we make use of the radial velocity axis of our CII data. In general, we can expect that ionizing or mechanical impacts from our non- $\theta^1$  Ori C stars will create movement in the local gas cloud. When the gas is accelerated along our line of sight, the CII emission appears stronger in the frame corresponding to its associated radial velocity.

#### 3.4.1 Spectral Averaging

For each of the identified regions of interest in our image, we are able to extract average spectra to look for local velocity structures. Average spectra are used to increase signal-noise in our data. This is done in one of two ways. First, for relatively small, localized regions of interest, we can simply take a circular mask with a radius larger than the region itself. We then create and compare three CII radial velocity spectra, one being the average spectrum of all the pixels that exceed our chosen cutoff value, and the other being the average spectrum of

the pixels that do not, and the last being the average spectrum over the whole region (see Figure B.2, Figure B.3 for example regions). In the case of large, uneven regions, we instead make two concentric masks, centered on the star(s) most likely to be causing the increased local radiation in the region. We can then compare the average spectrum of the inner region (the “very local area”), the average spectrum of the annulus between the two region boundaries, and the average spectrum of the entire outer region (see Figure B.1 and Figure B.4 for example regions).

In doing so, we are able to easily compare the very local velocity structure nearest the source of interest to the more general velocity structure of the nearby cloud. A good choice of region will look such that the average spectra of the pixels that are not in our region of interest (or the outer annulus) looks similar to the overall spectrum of the larger region. Larger velocity structures that warrant further research at this time will look very distinct from both of these. If the spectral averaging of a given region reveals a unique velocity structure in a region where this is not known or expected, we can do a deeper dive.

### 3.4.2 PV Diagrams

In cases where unique velocity structures are revealed by our region finding and average velocity techniques, we can create position-velocity (PV) diagrams to look further. This is very similar to the process conducted in Pabst et al. (2019) and Pabst et al. (2020). We start by dividing the region into small, horizontal cuts, each with a width of 70.5arcsec in declination (see Figure B.5). From there, we can integrate over declination and plot the right ascension vs the radial velocity for each region. Alternatively, the same can be done by taking vertical cuts and integrating over right ascension (see Figure B.6).

## 3.5 Bubble Formation Mechanism Analysis

If, from our previous analyses, we can well determine there exists a bubble in our region of interest, we then begin to attempt to categorize it. There are two basic mechanisms that contribute to the expansion of the bubbles we are looking for. The first involves increased pressure of a photo-ionized gas creating an outward gradient (Spitzer expansion) and the second is a mechanical stellar wind literally blowing the material away. As discussed in Pabst et al. (2020), M43 and NGC 1977 are Strömgren bubbles created under a primarily Spitzer-type expansion, and the Veil structure (driven by a much stronger O-type star) is primarily created via wind.

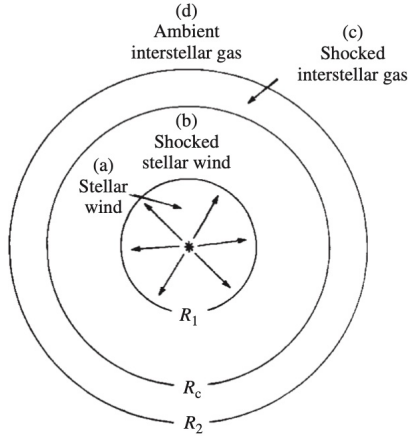


Figure 3.2 A schematic view of the shock process that creates stellar wind bubbles.  $R_1$  and  $R_2$  represent the locations of the two shocks, and  $R_c$  represents the discontinuity in the bubble shell.

### 3.5.1 Wind-Blown Bubble Evolution

O-type stars typically have powerful stellar winds (around 3000km/s), so powerful that they can literally blow bubbles in the surrounding medium. When the stellar wind interacts with the surrounding interstellar gas, at the location where the wind pressure ( $\rho_w v_w^2$ ) equals the thermal pressure of the surrounding gas, a shock in the opposite direction causes the wind to slow down. This will, in turn, induce a shock out on the ambient gas, causing it to be swept up. In the space between these two shocks, a discontinuity in pressure is formed, creating the bubble surface. Figure 3.2 (reproduced with permission from Tielens (2005) and originally found in Weaver et al. (1977)) shows a schematic view of this process.

If we have a strong enough understanding of the wind luminosity a given star, we then calculate the expected radius, age, and some information about the energy of the structures indicated, as done in Pabst et al. (2020). The process begins by estimating the radius (in arcsec) by reading it off the RA (or Dec) axis of the PV diagram. From here, this can be converted into a real distance (in pc) using right-triangle trigonometry, so long as the distance to the cloud is known. Similarly, the cloud velocity can be read from the radial velocity axis, and adjusting to account for the local standard of rest.

Additionally, the total mass of the bubble is simply going to be the total mass of all the material that was swept up in its creation. Therefore, if the initial gas mass density ( $\rho_0$ ) of the region is well known, finding the mass of the bubble

becomes simple, using the volume of the bubble.

$$m = \frac{4}{3}\pi r \times \rho_0$$

Finding the estimated age of the bubble is a little more difficult. For our purposes, we follow the logic in Chpt. 12.5 of Tielens (2005), which makes use of several equations from Weaver et al. (1977). Starting with the equation

$$r(t) \simeq 32 \left( \frac{L_w}{10^{36} \text{ ergs/s}} \right)^{1/5} \left( \frac{0.5 \text{ cm}^{-3}}{n_0} \right)^{1/5} \left( \frac{t}{10^6 \text{ years}} \right)^{3/5} \text{ pc}$$

where R is the cloud radius,  $L_w$  is the wind luminosity,  $n_0$  is the initial hydrogen number density, and t is the age. We can then rearrange to solve for the age:

$$t = \left[ \frac{R \text{ pc}}{32} \left( \frac{L_w}{10^{36} \text{ ergs/s}} \right)^{-\frac{1}{5}} \left( \frac{0.5 \text{ cm}^{-3}}{n_0} \right)^{-\frac{1}{5}} \right]^{5/3} \times 10^6 \text{ yr}$$

In the case of stars for which the wind luminosity or local initial number density is not well known, we can obtain an order-of-magnitude age estimate using the same equation for radius (in a slightly different form)

$$r(t) = \left( \frac{125}{154\pi} \right)^{1/5} \left( \frac{L_w}{\rho_0} \right)^{1/5} t^{3/5}$$

by establishing that

$$a = \left( \frac{125}{154\pi} \right)^{1/5} \left( \frac{L_w}{\rho_0} \right)^{1/5} = \frac{r}{t^{3/5}}$$

we can take the derivative, and plug in  $dr/dt = v$ :

$$v = a(3/5)t^{-2/5}$$

finally, plugging back in for  $a = \frac{r}{t^{3/5}}$  and solving for t, we get:

$$t = .6 \frac{r}{v}$$

Which only uses r and v, which can be read off the pv diagram.

From here, we can begin get an sense of what primary mechanism is causing the expansion of a given bubble (in reality, of course, it is likely that both predominant mechanisms may play a role). We start by comparing the bubble's kinetic energy with the expected wind energy of the star that blew it. The kinetic energy is calculated in the usual way

$$E_{kin} = \frac{1}{2}mv^2.$$

Where  $m$  and  $v$  are the mass and velocity of the bubble, respectively. In order to determine the wind energy of a given star, we can find the star's estimated mass loss rate ( $\dot{M}$ ) and wind velocity ( $v_w$ ) in the literature based on spectral type, and calculate its wind luminosity ( $L_w$ ) from that

$$L_w = \frac{1}{2}\dot{M}v_w^2.$$

Multiplying by the bubble age found above yields the wind energy exerted over the bubble's lifespan

$$E_w = L_w * t$$

From here, we take the ratio of these ( $E_{kin}/E_w$ ) and plot them against the bubble age as calculated above.

### 3.5.2 Spitzer-Type Bubble Evolution

In Strömgren spheres, the primary driving force of expansion is a pressure differential between the ionized gas in the HII region and surrounding unionized gas. As described in Chpt. 12.2 of Tielens (2005), following a rapid initial ionization phase, the ionization front between the HII and surrounding regions become very thin. When the degree of ionization changes so rapidly as one moves out, the increased temperature and pressure of the ionized gas (as compared to the neutral gas) can induce a shock into the surrounding medium. This shock will simultaneously increase the density in the surrounding medium while decreasing the density of the HII region. This decreased density will reduce the number of photons required to keep the region ionized, allowing more through, and pushing the ionization front further out. The shell between the ionization front and the shock front is what is observed as our expanding bubble.

An easy way to see if it is generally possible that a given bubble structure is by plotting it on a Spitzer diagram, which plots the shell velocity against the Spitzer-normalized mass. We start with a general equation for the mass of the bubble, similar to that described above, but now specifically accounting for the initial bubble radius.

$$m = \frac{4}{3}\pi\rho_o(r(0) - r(t))$$

From here, we can plug in the Strögen relation for initial density

$$\frac{4\pi}{3}n_0^2r(0)^3\alpha_B = N_{lyc}$$

(where  $n_0$  is the initial Hydrogen number density,  $\alpha_B$ , the radiative recombination coefficient (excluding the ground-state recombination), and  $N_{lyc}$ , the ionizing photon luminosity) and the velocity size equation

$$\frac{r(t)}{r(0)}(CII/v)^{4/3}$$

to get the equation for reduced mass

$$m/(\mu m_h N_{lyc}/\alpha_B) = (1/n_0)((CII/v)^4 - 1)$$

By taking the mass of the hydrogen atom ( $m_h$ ), the hydrogen reduced mass ( $\mu$ ),  $N_{lyc}$ , and  $\alpha_B$  from the literature, plus the actual bubble mass as calculated above, the left hand side of this equation gives us the reduced mass. From here, this (along with the velocity read from the PV diagram) can be plotted on a Spitzer diagram.

Chapter **4**

# Results and Discussion

## 4.1 Identified Regions of Interest

Our modeled radiation field ratio map (using the CII data WCS) can be found in Figure 4.1. This represents the map without  $\theta^1$  Ori C divided by the full map, such that a lower ratio indicates greater radiation domination by  $\theta^1$  Ori C. As is expected, we see a general trend wherein the very central M42 region is most strongly dominated by  $\theta^1$  Ori C, dropping off as one moves away from the star. Some very clear, bright yellow regions can be seen. It should be noted that the large majority of the region has a radiation field ratio greater than 0.5, meaning more than half the modeled field strength comes from other stars. While this doesn't account specifically for *ionizing* radiation, it still seems to imply that the radiation from  $\theta^1$  Ori C is not so completely dominant as we generally state.

From our modeled radiation field ratio map, we successfully mask out areas of the map where the radiation field is greater than a given cutoff value. A selection of masks with varying cutoff values are shown in Figure 4.2. We once again see that the vast majority of the map has a ratio greater than 0.5, and still a significant amount remains greater than 0.75. For the purposes of our analysis, we choose to utilize the mask with a 0.95 cutoff. Of all the values tested, this map gives us a reasonable distinction between regions of interest, without losing regions of possible significance nearest  $\theta^1$  Ori C. In doing so, we admittedly lose some specificity in the NGC 1977 region of the map. That being said, this region has already been fairly well studied, and is not a central point of interest for our purposes. It should be noted that the relatively large region in NGC 1977 seen in the 0.99 cutoff mask was used to center our circular mask when doing an average spectral analysis of the region (section 4.3).

In searching for areas of interest for study by comparing modeled radiation field maps, we uncover 5 primary regions of interest (Figure 4.3). Two of these,

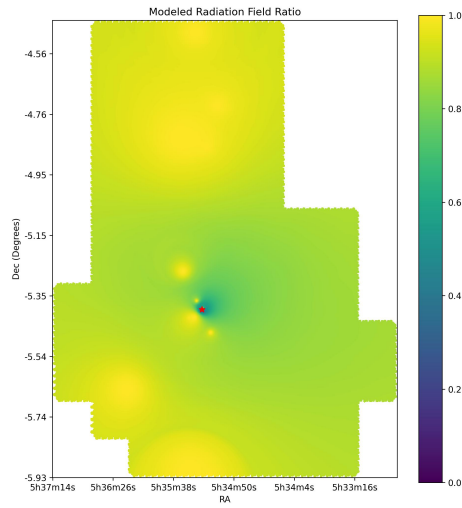


Figure 4.1 The map of modeled radiation field ratios. The location of  $\theta^1$  Ori C is denoted by the red star.

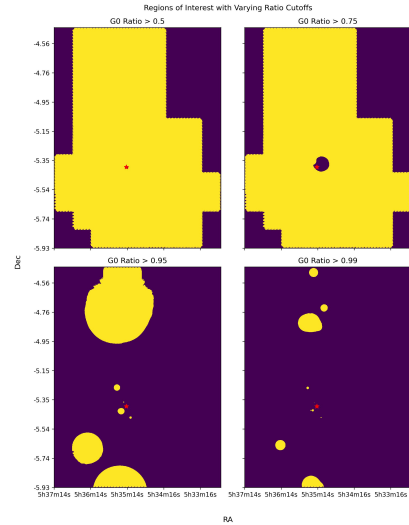


Figure 4.2 Four example ratio maps using the CII data WCS with cutoff values .5, .75, .95, and .99. Yellow regions are potential regions of interest. The red star marks the location of  $\theta^1$  Ori C

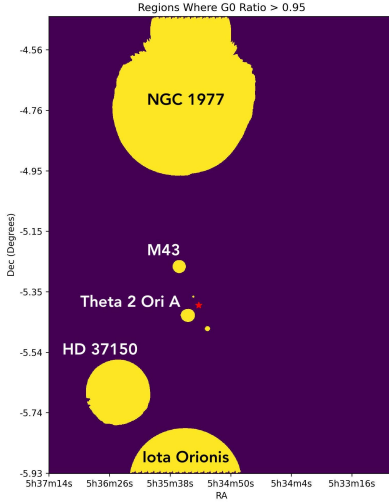


Figure 4.3 The ratio mask used in our CII data analyses, with identified regions of interest labeled.

NGC 1977 and M43, (section 4.3 and section 4.4) were very much expected, and have been extensively studied already (Pabst et al., 2020). The region surrounding  $\theta^2\text{Ori}\text{A}$  (section 4.5) has not been as extensively studied, but is still reasonably well expected. It is also of interest that even an area so close to  $\theta^1\text{Ori}\text{C}$  is still able to be picked up by this method of region-finding. The region surrounding HD 37150 was not at all expected, and therefore yields some interesting results (section 4.6). The last region, surrounding Iota Orionis, would be very interesting for further study, but the star's location at the edge of the data field makes this remarkably difficult at this time.

We repeat this region-finding step using the WCS of the Herschel temperature map (section 2.3), and find very similar regions of interest. The primary differences being the blending between the Iota Orionis and HD 37150 regions, and the existence of a new region in the upper right-hand corner. The latter is the result of the Herschel data being much larger originally, then cropped. There is a B star in the northwest corner of this region, that is not caught on the CII map because of where it cuts off (see Figure 2.1). The blending of the two southernmost regions is simply the result of the higher resolution of the Herschel map, possibly aided by the randomness in the scoby code described in 3.1.1.

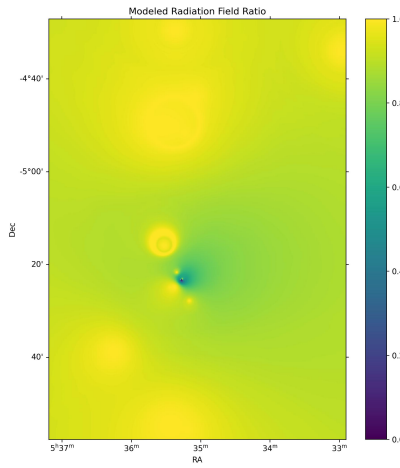


Figure 4.4 The ratio map of the temperature data. As was true with the CII data, much of the region has a ratio value greater than 0.5.

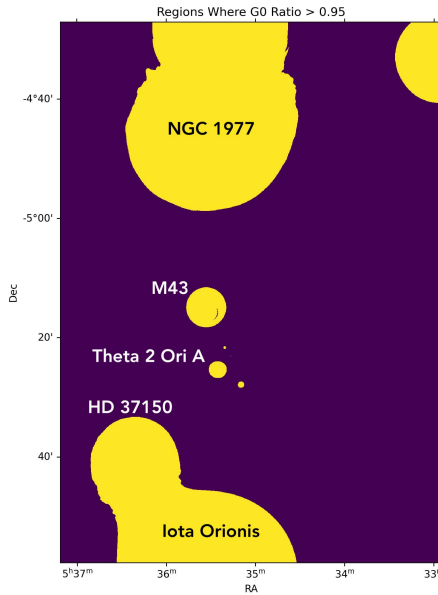


Figure 4.5 The region mask associated with the ratio map in Figure 4.4, with regions of interest labeled. An additional region is plainly visible in the northwest corner of the image. A cutoff value of 0.95 is used.

## 4.2 Whole-Field Analysis

We begin by conducting a short analysis of the entire Orion Nebula area for both the temperature data and the integrated CII data, comparing the regions of interest outlined above with rest of the map. This is done in two primary ways: first, we look at scatter plots to see if there is any difference in general trend in the real data vs. the modeled radiation field between these different areas. Second, we construct a histogram of data values for each set of pixels.

### 4.2.1 Integrated CII Data

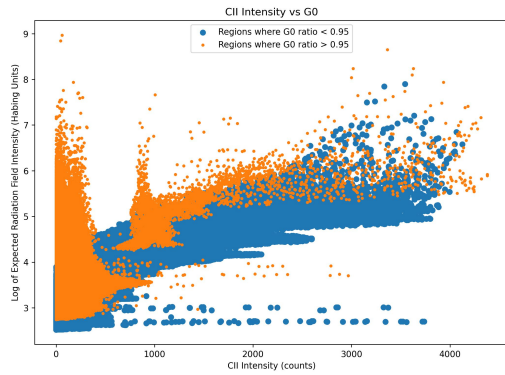


Figure 4.6 A scatterplot of the CII integrated data vs. expected radiation field intensity for both the regions of interest (orange) and the rest of the map (blue). Error bars in radiation field intensity are too small to be seen. Note that the Y-axis is in log scale to better show the trend.

The integrated CII data whole-field scatter plot (Figure 4.6) shows the same general trend for both regions above and below our cutoff value. Generally, in places where the measured CII intensity is higher, so, too is the modeled radiation field strength.

Of particular note, however are two sharp large “spikes” in the data from the regions of interest, and a similar, more diffuse spike in both data sets at the higher end of CII data counts. These represent areas on the map where the modeled radiation field strength is higher than expected, given the CII data values. By using the circular maps outlined in section 4.3 and section 4.4, we are able to show that these two spikes in our regions of interest clearly correspond to data in the NGC 1977 Figure 4.7 and M43 regions. By extension, we can presume the large, diffuse spikes correspond with the M42 area.

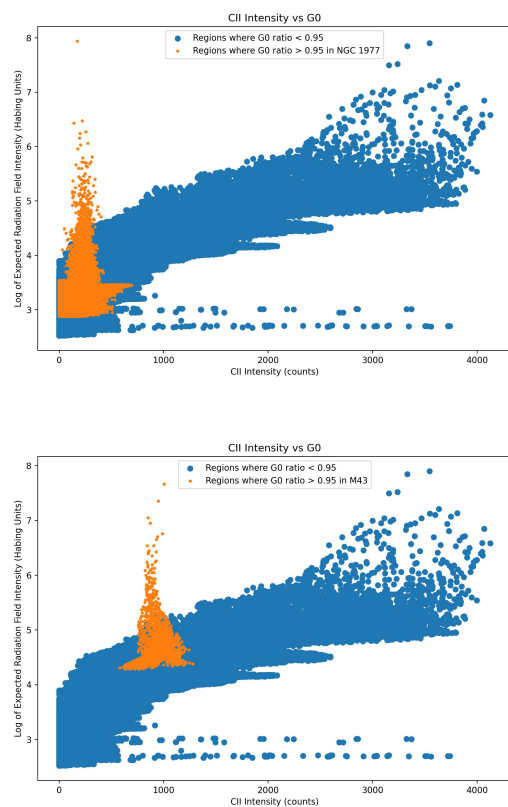


Figure 4.7 The same plot as Figure 4.6, but now with the region of interest data limited to the NGC 1977 (top) and M43 (bottom) regions. It is clearly shown that the spikes are correlated with these regions.

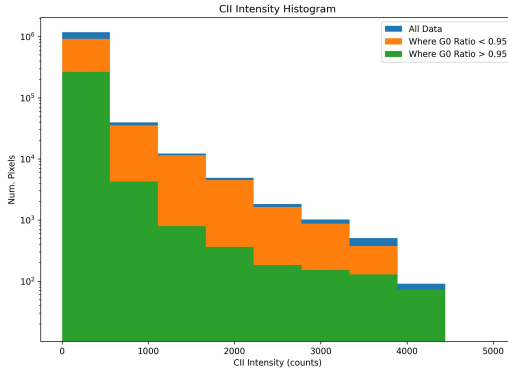


Figure 4.8 A histogram of CII data values for the regions of interest (green), the regions not-of-interest (orange), and the total data map (blue). Note that the counts axis is in log scale to better showcase the data.

We believe the fact that the scoby code does not account for gas or dust structure to be the cause of these spikes. In reality, the dust obscures the CII emission, causing it to look dimmer in regions with higher expected radiation field. This effect is clearly more pronounced in very active regions. We only see one spike in the data for regions not-of-interest because the only particularly active, dusty region in that data will be in M42.

Our histogram (Figure 4.8) of CII data values looks generally as we'd expect, with a strong right skew—there are a lot of pixels with very few counts, and very few pixels with high counts. It should be noted that there appear to be relatively fewer pixels with mid-range counts ( $\sim 1500$  to  $3000$ ) in the regions of interest, when compared to the other histograms. This is likely a result of the influence of  $\theta^1 Ori C$  extending out further than the influences of other stars, allowing for more mid-range ionization in far-out regions.

### 4.2.2 Temperature Data

The scatter plot for the Herschel temperature map (Figure 4.9) shows much the same patterns as noticed in the CII scatter plot. In general and as expected, the gas temperature and modeled radiation field strength are positively correlated. There are again several spikes in the region-of interest data as a result of the scoby code not accounting for gas structure. The first two come from NGC 1977 and M43 respectively, with the third most likely coming from the northwestern region that is not caught in the CII data, as described in section 4.1.

Our histogram for the temperature data also looks largely as expected. It

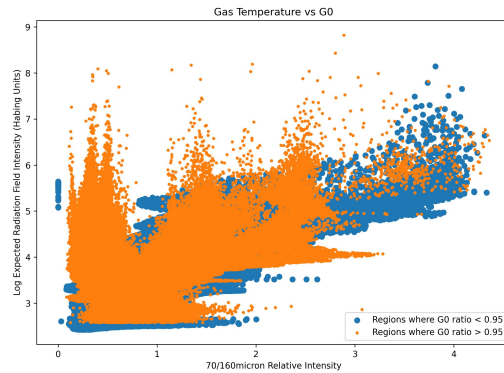


Figure 4.9 A scatter plot of general temperature proxy vs. modeled radiation field strength. Three spikes, corresponding with NGC 1977, M43, and the extra northwest region, are shown in the region-of-interest (orange) data. A spike corresponding to the M42 region is seen in the other (blue) data. Note that the y-axis is in log scale to better visualize the general trend

exhibits a clear right skew, with a maximum around a 0.75 ratio. This makes sense, as we expect the ambient gas to generally have a small, but nonzero temperature. The regions of interest seem to have relatively fewer points with very high temperature. This is most likely a result of  $\theta^1$  Ori C being so much hotter than the stars that form the other regions.

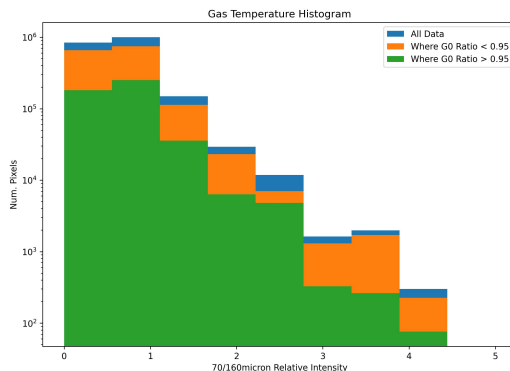


Figure 4.10 A histogram of temperature proxy values for the regions of interest (green) the regions not-of-interest (orange) and the entire map as a whole (blue). Note that the counts axis is in log scale for ease of viewing.

## 4.3 NGC 1977

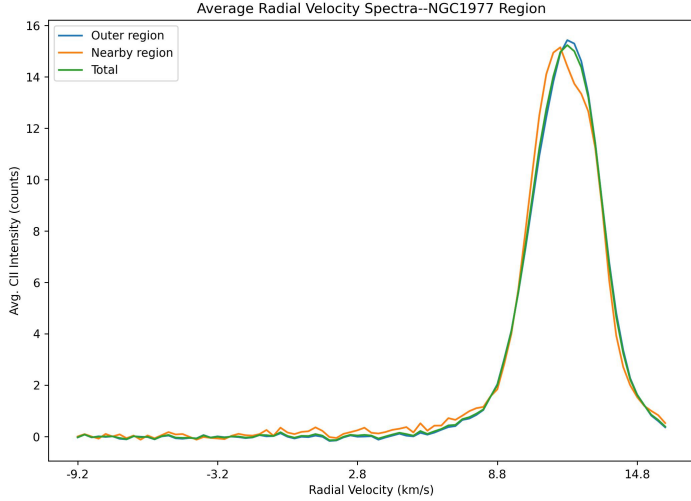


Figure 4.11 The averaged velocity spectra in the nearby (orange) outer (blue) and total (green) regions. A clear velocity structure can be seen near the peak of the nearby spectrum.

Now that we have completed a preliminary analysis of the overall field, we can focus in on our specific regions of interest. The first of these, NGC 1977, has been extensively studied, and its structure analyzed in detail in Pabst et al. (2020). We begin by taking concentric circular regions of this area centered on 42 Ori (Figure B.1) and averaging the CII radial velocity spectra over the inner circular region, the outer annular region, and the overall large region.

Looking at the average spectra in this area (Figure 4.11), we are able to see clear velocity structure in the nearby region. In this case, this structure looks like a small “dent” or skew near the very peak of the spectrum. This same structure is seen in the equivalent plot in Fig. 16 in Pabst et al. (2020). Because of the extensive analysis of this region done in Pabst’s work, we choose not to expand upon this region further at this time. Our result here, however, does serve to help show the efficacy of our modeled radiation field region-finding method.

## 4.4 M43

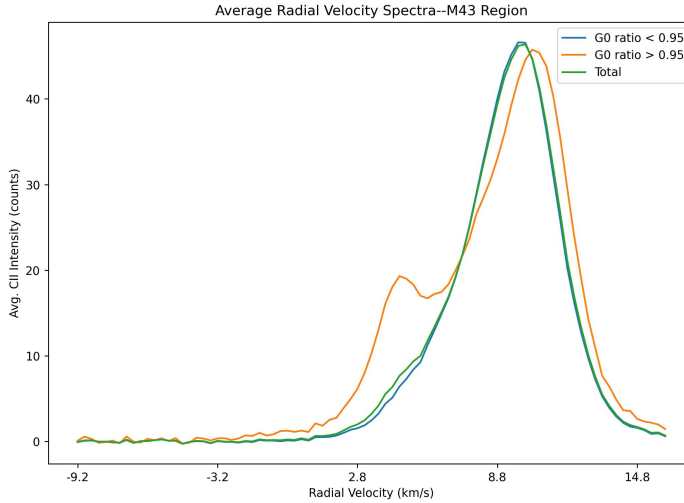


Figure 4.12 The average spectra for M43. The green line represents an average of the region outlined by the green circle in Figure B.2, the orange line represents an average of the subset of pixels in this circular region with radiation field ratio  $\zeta > 0.95$ , the blue line represents the average of other pixels in the circular region. There is a clear blue-shifted velocity spike is seen in the spectrum corresponding to the region of interest. Additionally, the primary peak of this spectrum appears to be slightly redshifted compared to the rest of the region.

We apply a similar process to analyzing the M43 region, but this time use a singular, smaller circular region, and dividing it between pixels above and below the cutoff value in our modeled radiation field ratio map (Figure B.2). This is preferable due to M43's relative proximity to  $\theta^1$  Ori C, as it allows us to select a smaller area.

Our averaged spectra of this region shows two primary velocity features, the first is a strong secondary peak in the region-of-interest spectrum at a radial velocity  $v_{LSR} \approx 4.5 \text{ km/s}$ . The second is the apparent redshift in the primary peak of the region-of-interest spectrum. This is indicative of a bubble structure in this region that is unable to expand as quickly on the redshifted side, blending the redshifted secondary peak with the primary peak. According to the literature, this is likely due to a difference in gas pressure from the OMC1 structure behind the bubble.

Like NGC 1977, M43 is very thoroughly analyzed in Pabst et al. (2020). It

should be noted that our average spectrum for the nearby region shows the velocity structure considerably more clearly than the average spectrum in Fig. 11 of this paper. This is a result of a difference in choice of the field that is being averaged over. Pabst chooses to average over the eastern limb-brightened shell, while we use a larger region. This is, however, a very strong indicator that our radiation field model region-finding method is very effective in picking out regions of interest where these structures may exist. Pabst et al. (2020) pulls this structure out more clearly in Fig. 13, which looks at spectra along horizontal cuts in this region. Once again, because of the extensive analysis of this structure that already exists in the literature, we choose not to expand further at this point in time. Once again, however, this serves as great evidence that our region-finding method works as expected.

## 4.5 $\theta^2$ Ori A

The next large region of interest picked up by our radiation field masking method is the area immediately surrounding  $\theta^2$  Ori A. This region is interesting, as its proximity to  $\theta^1$  Ori C in the Veil makes it relatively more difficult to study and model. It was for some time believed that the  $\theta^2$  association was not actually connected to the Orion Nebula in a meaningful way (Peimbert, 1982), but more recent studies (O'Dell et al., 2017) disagree. Additionally, there is indication that  $\theta^2$  Ori A is the dominant source of ionizing radiation in the entire region to the southeast of the bright bar structure (O'Dell et al., 2017). Again, this presents an example of how the gas structure of a cloud may impact the modeled radiation field region-finding method. Our region of interest indicated by our ratio map is more localized than the results of O'Dell et al. (2017). In any case, however, we are still able to generally identify the potential impact of  $\theta^2$  Ori A in the localized region.

We begin our analysis of the region similarly to M43, with a small, singular circle mask, centered around  $\theta^2$  Ori A (Figure B.3). The inner yellow pixels in this region are our very local region, while the outer purple pixels represent the local background.

Integrating over our regions in the same way as before (Figure 4.13), we are able to see a few things of note. The first being that the primary peak of the average spectrum is much higher in the very local region than in the general background. This is most likely a result of variations in gas density in the region. We are also able to see the redshifted feature in the background and whole region spectra that is indicative of the Veil structure (see Fig. 3 in Pabst et al. (2020)). Of interest, is the way our very localized spectrum is distinct from these. We see a similar structure in the very localized spectrum, but offset by a

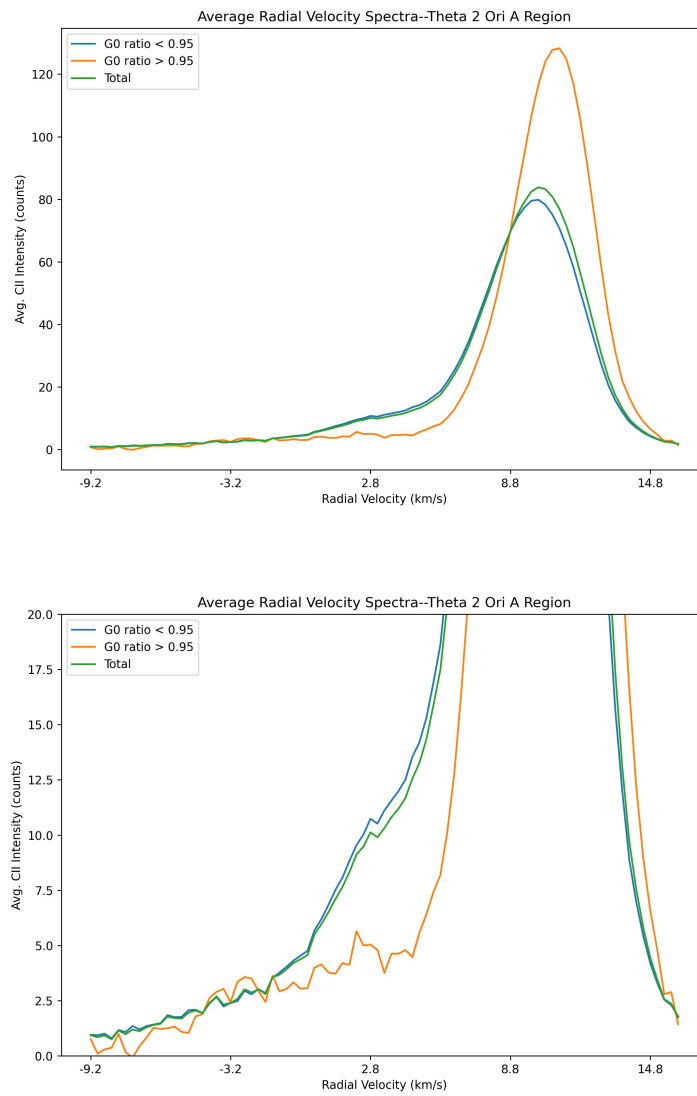


Figure 4.13 The averaged velocity spectrum near  $\theta^2$  Ori A. The full image (top) shows an offset in the Veil velocity structure for the very local case, as well as a general redshift in the main peak. A zoomed-in version (bottom) accentuates the difference in blueshifted features

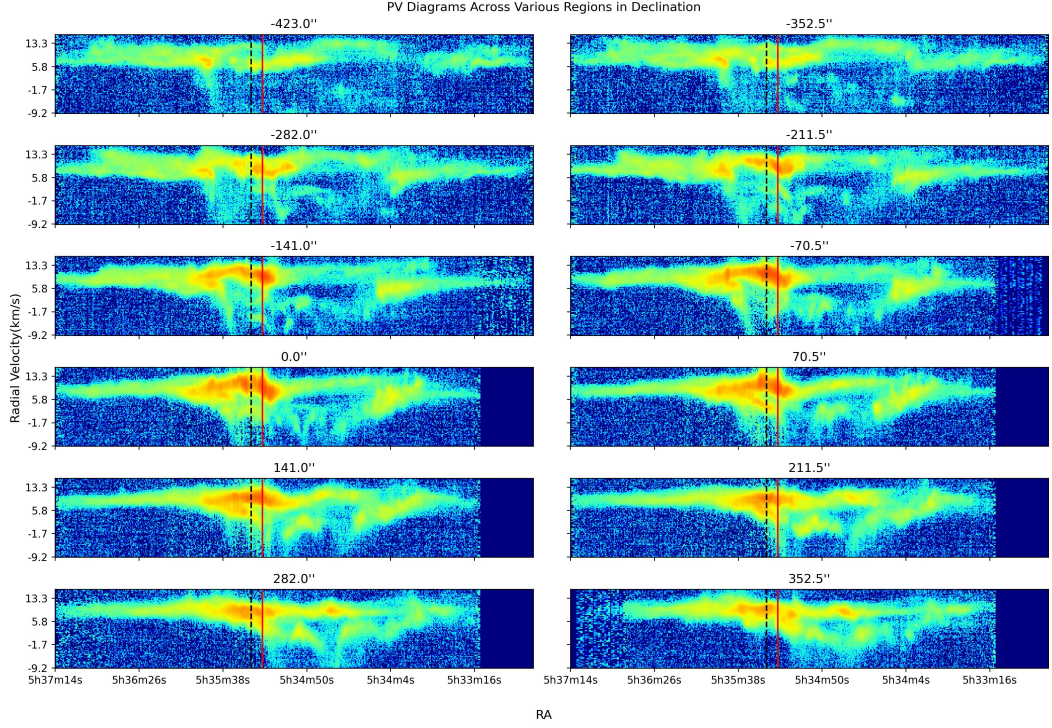


Figure 4.14 The PV diagrams for the  $\theta^2$  Ori A region. The red line marks the RA coordinate of  $\theta^1$  Ori C, and the black dotted line marks the RA coordinate of  $\theta^2$  Ori A. Subplot titles represent the angular distance offset (in arcsec) the central declination of each cut is from  $\theta^2$  Ori A. Meaning, the subplot labeled “0.0” corresponds to the cut that contains  $\theta^2$  Ori A.

visible amount. Additionally, we can see that the primary peak appears slightly blueshifted compared to the background.

Previous literature (van der Werf et al. (2013) and Pabst et al. (2020)) briefly recognizes a possible shell structure surrounding  $\theta^2$  Ori A, and these features in the velocity spectra are additional evidence that such a structure may exist. In order to probe further, we create a series of horizontal PV diagrams (Figure 4.14), similar to those created in Pabst et al. (2020), but by taking cuts in the more immediate region of  $\theta^2$  Ori A, in order to try to minimize blurring from the shell (Figure B.5).

These PV diagrams clearly show the large, redshifted bubble structure of the Veil on the right-hand side. This location is in line with what is observed in Pabst et al. (2019). As expected, in this region, we see some disruption in the velocity structure of the Veil, perhaps similar to the fossil outflows discussed in Kavak et al. (2022b), as we are so near the busiest part of the Orion Nebula.

Nearer the location of  $\theta^2$  Ori A, we see a particularly bright region that appears to be slightly blueshifted, in line with the increased maximum and offset in the primary peak seen in the very local spectrum of Figure 4.13. We can also see a very clear redshifted structure around the same radial velocity. In the diagrams corresponding to cuts just at and above  $\theta^2$  Ori A, this structure is particularly strong. This gives a strong indication that a unique bubble may exist around  $\theta^2$  Ori A, justifying further analysis.

### 4.5.1 Further Bubble Analysis

In order to assess the possible bubble formation mechanism in this region as described in section 3.5, we can begin by using the PV diagram highlighted in Pabst et al. (2019) (Figure 4.15). This diagram clearly and cleanly shows the greater Veil structure. Additionally, however, the Veil structure shown also seems to have a small inflection in the same region where we see our bubble structure in Figure 4.14. We believe this inflection is due to the influence of  $\theta^2$  Ori A, and is representative of its own bubble.

In terms of studying the bubble structure, we can make use of these diagrams. By estimating the ratio of radii between the two bubbles, we can more quickly estimate the radius and mass of  $\theta^2$  Ori A by using the values calculated for the Veil in Pabst et al. (2020). We measure the radius of the inflection region to be 1/3 that of the overall Veil value (about  $0.9\text{ pc}$ ), meaning the mass will be 1/9th that of the Veil (about  $55.5M_{\odot}$ ). We can also read the radial velocity relative to local standard of rest to be  $v_{LSR} \approx -2\text{ km/s}$ , giving an expansion velocity of  $v \approx 10\text{ km/s}$ . The other values related to the star and cloud structure can be found in Table 4.1. It should be noted that  $n_0$  is a free parameter in Storey & Hummer (1995), and our value was also picked with insight from Pabst et al. (2019). Additionally, the  $v_w$  value in the literature for  $\theta^2$  Ori A is not well determined.

From here, we calculate the age, normalized mass, and energy ratio as described in section 3.5 (see Table 5.1 for values), and plot our data on our Energy Ratio (Figure 4.16) and Spitzer Expansion (Figure 4.17) diagrams. We plot this bubble alongside the values for various well-studied bubbles from Pabst et al. (2019), Luisi et al. (2021), Tiwari et al. (2021), and Bonne et al. (2022).

Our energy-ratio diagram shows that  $\theta^2$  Ori A sits within a general trend with the other data that younger bubbles tend to have higher energy ratios. NGC 1977 and M43 are not seen in Figure 4.16. This is because these structures are Spitzer-type expansions, and as a result have energy ratios on the order of  $10^1$ . Given that we expect the  $\theta^2$  Ori A bubble to be a wind-blown type, it is odd that the energy ratio calculated is greater than 1. This is especially true given

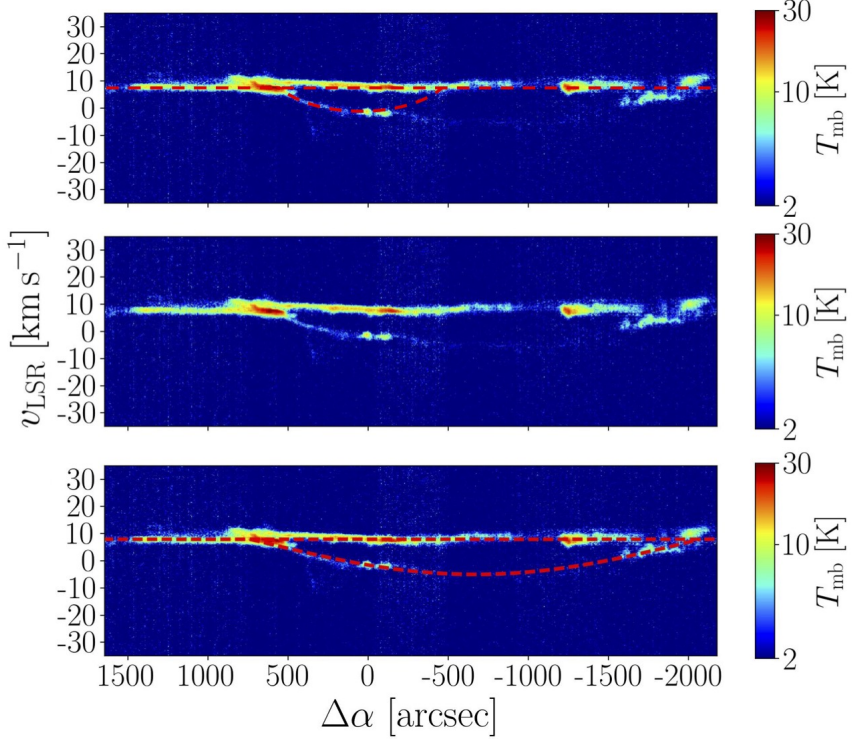


Figure 4.15 A PV diagram showcasing the Veil structure. The bottom two panels of this figure represent the second panel of Fig. 2 in Pabst et al. (2019). The central panel showing the PV diagram without additional annotation, and the bottom showing it with lines highlighting the horizontal location of the cloud and the structure of the Veil. The top panel represents similar information, but if we were to try to fit just the part to the left of the inflection, the region of possible influence by  $\theta^2$  Ori A. Reproduced with permission.

Table 4.1. Characteristics Used in Bubble Analysis

	r (pc)	m ( $M_\odot$ )	$N_{lyc}$ ( $s^{-1}$ )	$\alpha_b$ ( $cm^3/s$ )	$n_0$ ( $cm^{-3}$ )	$\dot{M}$ ( $M_\odot/yr$ )	$v_w$ (km/s)
Value	0.9	55.5	$2.3 \times 10^{48}$	$3.3 \times 10^{-13}$	2000	$3.16 \times 10^{-8}$	700
Source	–	–	1	2	2	3	3

<sup>1</sup>Vacca et al. (1996)

<sup>2</sup>Storey & Hummer (1995)

<sup>3</sup>Howarth & Prinja (1989)

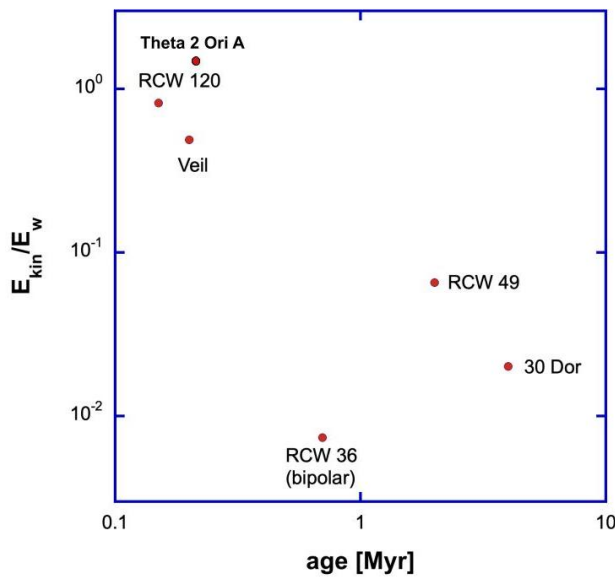


Figure 4.16 The energy ratio diagram, with data from various well-studied bubbles. It should be noted that the  $E_{\text{kin}}/E_w$  values for NGC 1977 and M43 are on the order of  $10^1$ , so would exist above the limits of the y axis. Additional data comes from Pabst et al. (2019), Luisi et al. (2021), Tiwari et al. (2021), and Bonne et al. (2022).

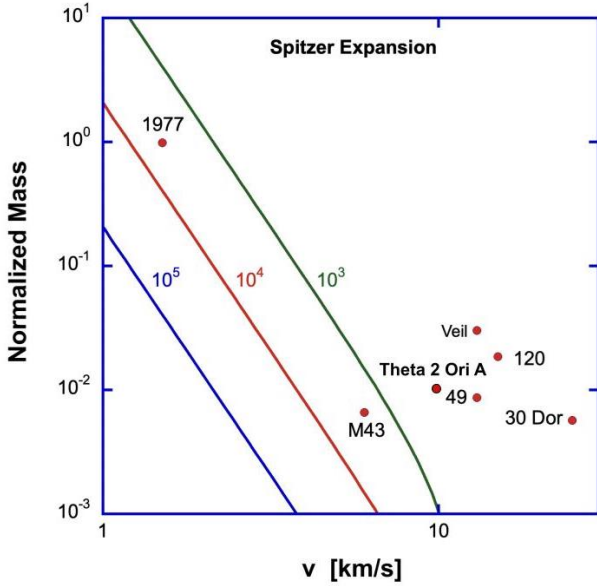


Figure 4.17 The Spitzer diagram, with data from various well-studied bubbles. The diagonal lines represent different ambient densities. Additional data comes from Pabst et al. (2019), Luisi et al. (2021), Tiwari et al. (2021), and Bonne et al. (2022).

that its location on the Spitzer diagram (Figure 4.17) and spectral type indicate that it is very unlikely that this structure is the result of a Spitzer expansion. Similar analysis of the apparent irregularity can be found in Price et al. (2001).

There are a few possible explanations for this odd placement. The first (and most unlikely) is that we are simply overestimating the expansion velocity of the bubble. This, however, is a value read straight from the PV diagram, and if wrong, would indicate systematic issues with the currently accepted value for the expansion velocity of the Veil, which has been well founded (Pabst et al., 2020). Additionally, a similar observation of this apparent irregularity is also found in Price et al. (2001). As the stellar wind velocity taken from Howarth & Prinja (1989) is not well determined, there is a possibility that the wind energy ( $E_w$ ) is being underestimated. However, as  $\theta^2$  Ori A is still only an 09.5 star, it seems unlikely this would fully account for this issue. It seems more likely that this strange placement is the result of additional energy input from  $\theta^1$  Ori C accelerating the redshifted part of the bubble. Alternatively, it is also possible that  $\theta^2$  Ori A's relatively large radial velocity (8 km/s relative to the cloud), is altering our observations in a way that is not accounted for in more simple modeling. An analysis of a similar system can be found in Luisi et al. (2021). It

should be noted, however, that this relatively high radial velocity is not especially unique to  $\theta^2$  Ori A (Da Rio et al., 2017), and is therefore *not* an indication that this star is somehow separate from the rest of the cluster.

## 4.6 HD 37150

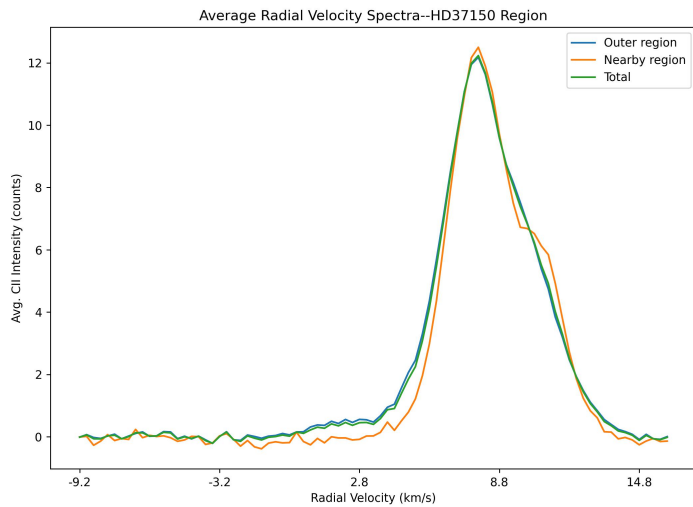


Figure 4.18 The average velocity spectra of regions surrounding HD 37150. The very nearby region (orange) shows a clear redshifted feature not present in the outer region (blue) or entire area (green).

The last region of interest that was identified by our radiation field ratio method (and is well enough within the frame of our CII data for further analysis) is the area immediately surrounding HD 37150. HD 37150 is a star of B3 spectral class, and is therefore relatively weak compared to  $\theta^1$  Ori C and  $\theta^2$  Ori A. As a result, it has not been as extensively studied in terms of its impact on the surrounding medium. As done previously, we start by taking an average velocity spectrum for the very near region, the outer region, and the entire immediate area using the circular masks outlined in Figure B.4.

Because of the relatively large size of the outermost region used (Figure B.4), the blueshifted side shows a slight feature that is expected to be a result of the veil. More surprising, however, given the relatively weak nature of HD 37150, is the clear redshifted feature on the opposite side. This feature most strongly appears in the very nearby region, and is therefore most likely associated with

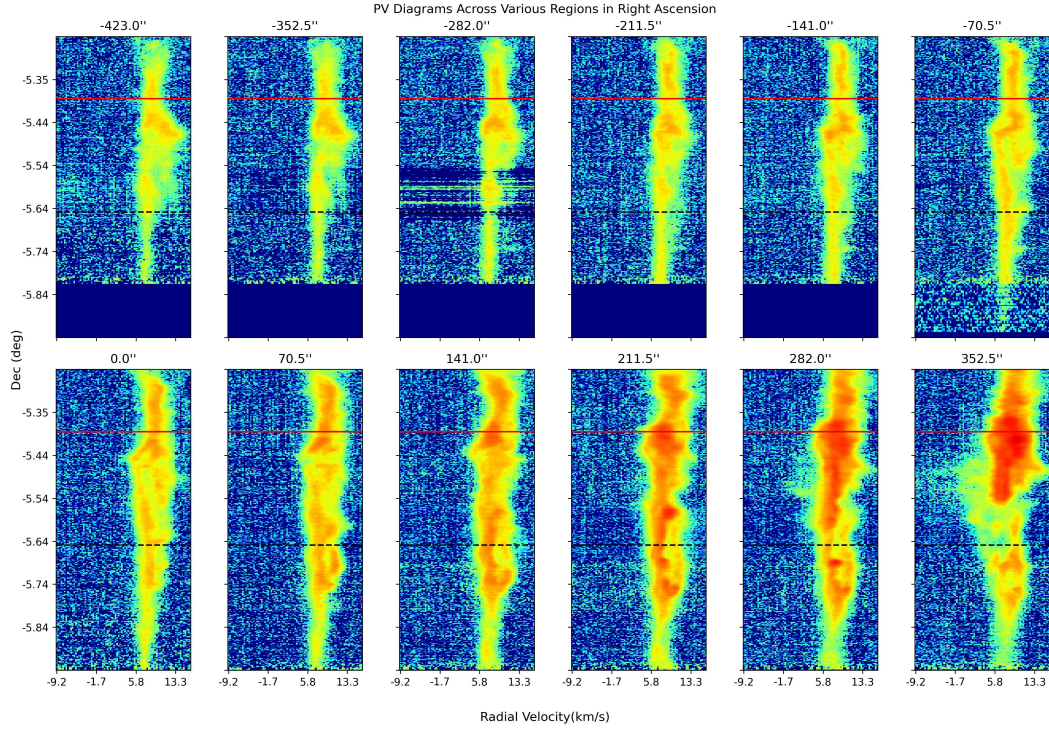


Figure 4.19 The PV diagrams for the region surrounding HD 37150. The red line represents the declination position of  $\theta^1$  Ori C, while the black dotted line represents HD 37150. Subplot titles indicate the associated region center's offset in right ascension (in arcsec). Colors are in log scale.

HD 37150, and not a result of the star's relatively close position to the Orion A cloud.

As was true before, our next step is to create PV diagrams (Figure 4.19) to get a greater sense of the structure of this velocity feature. However (as was shown in the spectra) this region is not totally independent from influence from the greater veil structure. We observe that taking vertical cuts for our PV diagrams (Figure B.6) and integrating over right ascension is more effective at separating this influence. The cuts chosen are, again,  $\sim 70.5$  arsec wide each.

In doing so, we can see a redshifted structure form in the PV diagrams associated with the location HD 37150 and nearby area. It should be noted that the coordinates and parallax of HD 37150 indicate that it is probably more closely associated with Orion A than the M42 region. As a result, we can see that the cloud radial velocities is less clear in this image. This makes it relatively difficult to measure the radius or expansion velocity of the observed bubble. We can better see the span of this bubble by taking average spectra in several small,

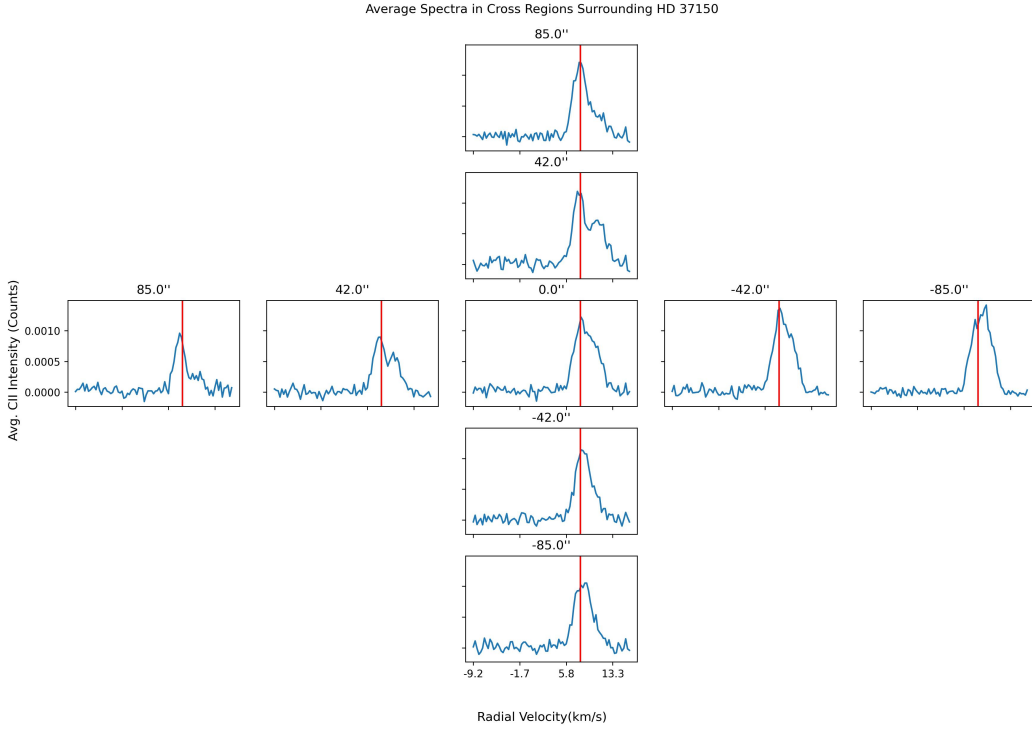


Figure 4.20 The average velocity spectra at regions near HD 37150. Each is the average over a circle with diameter  $\sim 42$  arcsec, and is offset by the same amount. Subplot titles represent the central offset from the location of HD 37150. The red vertical line represents the radial velocity of the M42/OMC1 cloud.

circular regions (Figure B.7), each with a diameter  $\sim 42$  arcsec, in a cross shape centered on HD 37150.

Using this and the general average spectrum (Figure 4.18) of this area, we can roughly estimate that the angular radius of the bubble is between 42 and 85 arcsec, corresponding to radii of 0.07 and 0.15, at a distance of 377 pc (the distance to HD 37150), respectively. We can also find that its expansion velocity (i.e. the distance between the secondary structure peak and the primary cloud peak), is about 1.3 km/s. Further analysis as done in subsection 4.5.1 is not reasonably possible without greater understanding of the gas structure in Orion A.

In any case, for such a star with weak stellar wind and relatively low ionizing luminosity, this is apparently a *very* large bubble. As a result, we believe that the formation mechanism of this bubble can not be explained with the simple wind-blown and Spitzer models. It is possible, however that some very energetic effect early in the lifespan of HD 37150 released a lot of energy all

at once, creating the bubble. We speculate that this may very well be a fossil bubble, created as a result of protostellar outflow activity. It is interesting to note that, for this region, the redshifted side of the bubble is clearly the more distinct of the two. Most of the bubble structures studied in this region, particularly the veil, have stronger blueshifted features, as the high density of OMC1 in the background slows down the expansion on that side. We do not observe any particularly dense gas structure along the line of sight between us and HD 37150, so the cause of the lack of blueshifted feature is not certain. That being said, it is possible that such a feature may be “out-shined” by the Veil.

It is important to note that the Hipparcos catalog has HD 37150 as a strongly blueshifted star, with a radial velocity of  $v_{lsr} = -7.3$ . In reality, it has been shown that HD 37150 is in a binary system, and this strong apparent blueshift is a result of its binarity. Accounting for this, Morrell & Levato (1991) finds a radial velocity that is well within the realm of the greater cloud velocity.

# Chapter 5

## Conclusion

Ultimately, we are able to conclude that using modeled radiation field ratios is an effective way to determine possible regions of interest in gas cloud regions like that of the Orion Nebula. We show that this method was able to find several well-known and well-studied regions, as well as highlighting the region around HD 37150, which has not been analyzed so deeply thus far.

We also show that the regions picked out can be used for further study, and determine some characteristics for bubble structures surrounding  $\theta^2$  Ori A and HD 37150, our final results for these analyses are presented in Table 5.1.

### 5.1 Future Outlook

This study also lays the groundwork for possible future research in several ways:

- Given more extensive data in the region, it would be of interest to apply similar analysis to the Iota Orionis region found in the CII data, as well as the Northwestern region picked up in the Herschel data.
- A deeper dive into the separate regions picked out in NGC 1977 with the 0.99 radiation field ratio cutoff (Figure 4.2) may be interesting, perhaps this region has greater substructure than previously indicated
- A better understanding of the gas structure in Orion A near HD 37150 could be used to more deeply understand the bubble observed there, especially in relation to its possible formation mechanism around a relatively weak star.

Table 5.1. Bubble Characteristics

Driving Star	r (pc)	m ( $M_{\odot}$ )	t (Myr)	$L_w$ ( $L_{\odot}$ )	$E_w$ ( $10^{46}$ erg)	$E_{kin}$ ( $10^{46}$ erg)
$\theta^1$ Ori C	2.7	1500	0.2	400	500	250
NGC 1977	1.6	700	0.4	$1.5 \times 10^{-2}$	15	.3
M43	0.3	7	0.02	$1.5 \times 10^{-2}$	80	2
$\theta^2$ Ori A	0.9	55	0.24	1.2	3.7	5.5
HD37150	0.7-1.5	-	-	-	-	-

\*Value only constitutes an order-of-magnitude estimate.

- Further analysis of the impact of  $\theta^2$  Ori A in the cloud structure in the veil region.
- Finally, the application of our region-finding technique to cloud structures and nebulae that have not been as extensively studied as Orion could lead researchers to finding bubbles that we do not currently know about.

## 5.2 Acknowledgments

Special thanks to Dr. Alexander Tielens (professor, Leiden University) and his strong mentorship, without which this project would not have been possible. Thanks are also owed to Dr. Cornelia Pabst (postdoc, Leiden University) for her brilliant insight as well. Sincerest gratitude goes to Ramsey Karim (PhD candidate, University of Maryland, College Park) whose scoby code served as the foundation for this project. Additional thanks to Dr. Anthony Brown (professor, Leiden University) for his advisement. The author's participation in the Leiden University MSc Astronomy program is partially supported by the James B. Reynolds Scholarship for Foreign Study from Dartmouth College.

# Bibliography

- Abel, N. P., Ferland, G. J., & O'Dell, C. R. 2019, *ApJ*, 881, 130, doi: 10.3847/1538-4357/ab2a6e
- Abt, H. A. 2008, *ApJS*, 176, 216, doi: 10.1086/525529
- Bonne, L., Schneider, N., García, P., et al. 2022, arXiv e-prints, arXiv:2207.06479. <https://arxiv.org/abs/2207.06479>
- Burssens, S., Simón-Díaz, S., Bowman, D. M., et al. 2020, *A&A*, 639, A81, doi: 10.1051/0004-6361/202037700
- Churchwell, E., Povich, M. S., Allen, D., et al. 2006, *ApJ*, 649, 759, doi: 10.1086/507015
- Da Rio, N., Tan, J. C., Covey, K. R., et al. 2017, *ApJ*, 845, 105, doi: 10.3847/1538-4357/aa7a5b
- Gaia Collaboration. 2018, VizieR Online Data Catalog, I/345
- . 2020, VizieR Online Data Catalog, I/350
- Goicoechea, J. R., Teyssier, D., Etxaluze, M., et al. 2015, *ApJ*, 812, 75, doi: 10.1088/0004-637X/812/1/75
- Goicoechea, J. R., Pabst, C. H. M., Kabanovic, S., et al. 2020, *A&A*, 639, A1, doi: 10.1051/0004-6361/202037455
- Güdel, M., Briggs, K. R., Montmerle, T., et al. 2008, *Science*, 319, 309, doi: 10.1126/science.1149926
- Hainich, R., Ramachandran, V., Shenar, T., et al. 2019, *A&A*, 621, A85, doi: 10.1051/0004-6361/201833787

- Hamann, W. R., & Gräfener, G. 2004, *A&A*, 427, 697, doi: 10.1051/0004-6361:20040506
- Herbig, G. H. 1950, *ApJ*, 111, 15, doi: 10.1086/145233
- Hillenbrand, L. A. 1997, *AJ*, 113, 1733, doi: 10.1086/118389
- Houk, N., & Swift, C. 1999, Michigan Spectral Survey, 5, 0
- Howarth, I. D., & Prinja, R. K. 1989, *ApJS*, 69, 527, doi: 10.1086/191321
- Kavak, Ü., Bally, J., Goicoechea, J. R., et al. 2022a, *A&A*, 663, A117, doi: 10.1051/0004-6361/202243332
- Kavak, Ü., Goicoechea, J. R., Pabst, C. H. M., et al. 2022b, *A&A*, 660, A109, doi: 10.1051/0004-6361/202141367
- Leitherer, C., Schaerer, D., Goldader, J. D., et al. 1999, *ApJS*, 123, 3, doi: 10.1086/313233
- Levenhagen, R. S., & Leister, N. V. 2006, *MNRAS*, 371, 252, doi: 10.1111/j.1365-2966.2006.10655.x
- Luisi, M., Anderson, L. D., Schneider, N., et al. 2021, *Science Advances*, 7, eabe9511, doi: 10.1126/sciadv.abe9511
- Martins, F., Schaerer, D., & Hillier, D. J. 2005, *A&A*, 436, 1049, doi: 10.1051/0004-6361:20042386
- Mason, B. D., Gies, D. R., Hartkopf, W. I., et al. 1998, *AJ*, 115, 821, doi: 10.1086/300234
- Morrell, N., & Levato, H. 1991, *ApJS*, 75, 965, doi: 10.1086/191556
- Nesterov, V. V., Kuzmin, A. V., Ashimbaeva, N. T., et al. 1995, *A&AS*, 110, 367
- O'Dell, C. R., Ferland, G. J., & Peimbert, M. 2017, *MNRAS*, 464, 4835, doi: 10.1093/mnras/stw2713
- Pabst, C., Higgins, R., Goicoechea, J. R., et al. 2019, *Nature*, 565, 618, doi: 10.1038/s41586-018-0844-1
- Pabst, C. H. M., Goicoechea, J. R., Teyssier, D., et al. 2020, *A&A*, 639, A2, doi: 10.1051/0004-6361/202037560
- Peimbert, M. 1982, *Annals of the New York Academy of Sciences*, 395, 24, doi: 10.1111/j.1749-6632.1982.tb43375.x

- Poglitsch, A., Waelkens, C., Geis, N., et al. 2010, *A&A*, 518, L2, doi: 10.1051/0004-6361/201014535
- Price, R. J., Crawford, I. A., Barlow, M. J., & Howarth, I. D. 2001, *MNRAS*, 328, 555, doi: 10.1046/j.1365-8711.2001.04893.x
- Risacher, C., Güsten, R., Stutzki, J., et al. 2016, *A&A*, 595, A34, doi: 10.1051/0004-6361/201629045
- Sander, A., Hamann, W. R., & Todt, H. 2012, *A&A*, 540, A144, doi: 10.1051/0004-6361/201117830
- Sota, A., Maíz Apellániz, J., Walborn, N. R., et al. 2011, *ApJS*, 193, 24, doi: 10.1088/0067-0049/193/2/24
- Storey, P. J., & Hummer, D. G. 1995, *MNRAS*, 272, 41, doi: 10.1093/mnras/272.1.41
- Tielens, A. G. G. M. 2005, *The Physics and Chemistry of the Interstellar Medium* (Cambridge University Press), doi: 10.1017/CBO9780511819056
- Tiwari, M., Karim, R., Pound, M. W., et al. 2021, *ApJ*, 914, 117, doi: 10.3847/1538-4357/abf6ce
- Todt, H., Sander, A., Hainich, R., et al. 2015, *A&A*, 579, A75, doi: 10.1051/0004-6361/201526253
- Vacca, W. D., Garmany, C. D., & Shull, J. M. 1996, *ApJ*, 460, 914, doi: 10.1086/177020
- van der Werf, P. P., Goss, W. M., & O'Dell, C. R. 2013, *ApJ*, 762, 101, doi: 10.1088/0004-637X/762/2/101
- van Leeuwen, F. 2007, *A&A*, 474, 653, doi: 10.1051/0004-6361:20078357
- Walch, S., Whitworth, A. P., Bisbas, T. G., Wünsch, R., & Hubber, D. A. 2013, *MNRAS*, 435, 917, doi: 10.1093/mnras/stt1115
- Warren, W. H., J., & Hesser, J. E. 1977, *ApJS*, 34, 115, doi: 10.1086/190446
- Weaver, R., McCray, R., Castor, J., Shapiro, P., & Moore, R. 1977, *ApJ*, 218, 377, doi: 10.1086/155692
- Zari, E., Brown, A. G. A., de Bruijne, J., Manara, C. F., & de Zeeuw, P. T. 2017, *A&A*, 608, A148, doi: 10.1051/0004-6361/201731309

Appendix **A**

## Extended Tables

Table A.1. Stellar Data

Name	RA	Dec	Spectral Type	Parallax	Coordinate Source	Spectral Type Source	Parallax Source
1 HD 36917	05 34 14.5822	-05 34 14.583	B9III/IV	2.2200	Gaia Collaboration (2020)	Houk & Swift (1999)	Gaia Collaboration (2020)
2 HD 36865	05 34 32.4215	-04 29 14.790	B8V	3.5935	Gaia Collaboration (2018)	Houk & Swift (1999)	Gaia Collaboration (2018)
3 HD 36938	05 34 56.2378	-04 45 57.382	B9V	2.5121	Gaia Collaboration (2020)	Houk & Swift (1999)	Gaia Collaboration (2020)
4 HD 36998	05 35 13.2278	-04 35 40.989	B9V	3.1765	Gaia Collaboration (2020)	Houk & Swift (1999)	Gaia Collaboration (2020)
5 HD 294264	05 35 13.3447	-04 51 44.916	B3	2.4265	Gaia Collaboration (2020)	Nesterov et al. (1995)	Gaia Collaboration (2020)
6 42 Ori	05 35 23.1642	-04 50 18.088	B1V	3.6900	van Leeuwen (2007)	Burssens et al. (2020)	van Leeuwen (2007)
7 HD 37130	05 36 03.5675	-04 45 07.631	B8/9IV	2.5617	Gaia Collaboration (2020)	Houk & Swift (1999)	Gaia Collaboration (2020)
8 HD 36655	05 33 07.4754	-05 20 26.106	B9V	2.8153	Gaia Collaboration (2020)	Houk & Swift (1999)	Gaia Collaboration (2020)
9 $\theta^1$ Ori D	05 35 17.2574	-05 23 16.570	B1.5Vp	2.2820	Gaia Collaboration (2020)	Levenhagen & Lester (2006)	Gaia Collaboration (2020)
10 $\theta^1$ Ori F	05 35 16.7270	-05 23 25.197	B8	2.5502	Gaia Collaboration (2020)	Herbig (1950)	Gaia Collaboration (2020)
11 $\theta^1$ Ori A	05 35 15.8254	-05 23 14.334	B0V	2.6427	Gaia Collaboration (2020)	Warren & Hesser (1977)	Gaia Collaboration (2020)
12 HD 37060	05 35 34.2772	-05 06 21.214	(B9)	2.5792	Gaia Collaboration (2020)	Houk & Swift (1999)	Gaia Collaboration (2020)
13 HD 37114	05 35 38.5404	-05 22 31.373	B9V	3.0307	Gaia Collaboration (2020)	Houk & Swift (1999)	Gaia Collaboration (2020)
14 HD 37174	05 36 27.1856	-05 24 31.314	B9V	2.6328	Gaia Collaboration (2020)	Houk & Swift (1999)	Gaia Collaboration (2020)
15 $\theta^2$ Ori C	05 35 31.4311	-05 25 16.371	B4V	2.4513	Gaia Collaboration (2020)	Sota et al. (2011)	Gaia Collaboration (2020)
16 HD 36982	05 35 09.8363	-05 27 53.216	B1.5Vp	2.4489	Gaia Collaboration (2020)	Houk & Swift (1999)	Gaia Collaboration (2020)
17 HD 36958	05 35 04.7875	-04 43 54.626	B3/5V	2.7552	Gaia Collaboration (2020)	Burssens et al. (2020)	Gaia Collaboration (2020)
18 $\theta^2$ Ori A	05 35 22.9012	-05 24 57.832	O9.5Vp	2.9728	Gaia Collaboration (2020)	Houk & Swift (1999)	Gaia Collaboration (2020)
19 V* V1046 Ori	05 35 21.8667	-04 29 39.024	B2/3V	2.7835	Gaia Collaboration (2020)	Houk & Swift (1999)	Gaia Collaboration (2020)
20 HD 37058	05 35 33.3539	-04 50 15.181	B3/5II	2.6181	Gaia Collaboration (2020)	Houk & Swift (1999)	Gaia Collaboration (2020)
21 HD 36629	05 32 57.0824	-04 33 59.339	B2V	2.3310	Gaia Collaboration (2020)	Houk & Swift (1999)	Gaia Collaboration (2020)
22 HD 36939	05 34 55.2955	-05 30 22.104	B7/8II	2.3827	Gaia Collaboration (2020)	Houk & Swift (1999)	Gaia Collaboration (2020)
23 HD 37061	05 35 31.3649	-05 16 02.582	O9.5V	2.4059	Gaia Collaboration (2020)	Burssens et al. (2020)	Gaia Collaboration (2020)
24 Brun 818	05 35 40.1802	-05 17 29.396	B6	2.4567	Gaia Collaboration (2020)	Hillenbrand (1997)	Gaia Collaboration (2020)
25 V* V1073 Ori	05 35 28.4251	-05 26 20.350	B9.5V	2.6059	Gaia Collaboration (2020)	Mason et al. (1998)	Gaia Collaboration (2020)
26 HD 36981	05 35 06.1984	-05 12 15.917	B7III/IV	2.5947	Gaia Collaboration (2020)	Houk & Swift (1999)	Gaia Collaboration (2020)
27 $\theta^1$ Ori B	05 35 16.1339	-05 23 06.784	B1V	2.6548	Gaia Collaboration (2020)	Hillenbrand (1997)	Gaia Collaboration (2020)
28 V* V1230 Ori	05 35 20.7204	-05 21 44.345	B1	2.4554	Gaia Collaboration (2020)	Burssens et al. (2020)	Gaia Collaboration (2020)
29 $\theta^2$ Ori B	05 35 26.4007	-05 25 00.793	B0.7V	2.3870	Gaia Collaboration (2020)	Sota et al. (2011)	Gaia Collaboration (2020)
30 $\theta^1$ Ori C	05 35 16.4662	-05 23 22.921	O7Vp	2.5014	Gaia Collaboration (2020)	Houk & Swift (1999)	Gaia Collaboration (2020)
31 HD 37059	05 35 31.1580	-04 54 15.178	B8/A0V	2.5972	Gaia Collaboration (2020)		Gaia Collaboration (2020)

Table A.1 (cont'd)

	Name	RA	Dec	Spectral Type	Parallax	Coordinate Source	Spectral Type Source	Parallax Source
32	HD 36983	05 35 07.6307	-05 52 08.399	B5(II/III)	2.6335	Gaia Collaboration (2020)	Houk & Swift (1999)	Gaia Collaboration (2020)
33	HD 36999	05 35 14.0074	-05 49 36.276	B8(III)	2.6025	Gaia Collaboration (2020)	Houk & Swift (1999)	Gaia Collaboration (2020)
<b>34</b>	<b>HD 37150</b>	<b>05 36 15.0278</b>	<b>-05 38 52.514</b>	<b>B3III</b>	<b>2.6585</b>	Gaia Collaboration (2020)	Houk & Swift (1999)	Gaia Collaboration (2020)
35	HD 37000	05 35 11.0124	-05 55 36.881	B3/5	2.6184	Gaia Collaboration (2020)	Houk & Swift (1999)	Gaia Collaboration (2020)
36	<i>l</i> Ori	05 35 25.9819	-05 54 35.643	O9IIIvar	1.4000	van Leeuwen (2007)	Sota et al. (2011)	van Leeuwen (2007)
37	<i>l</i> Ori B	05 35 26.4561	-05 54 44.447	B8III	2.7870	Gaia Collaboration (2020)	Abt (2008)	Gaia Collaboration (2020)

# Appendix B

## Extended Figures

### B.1 Averaged Spectra Regions

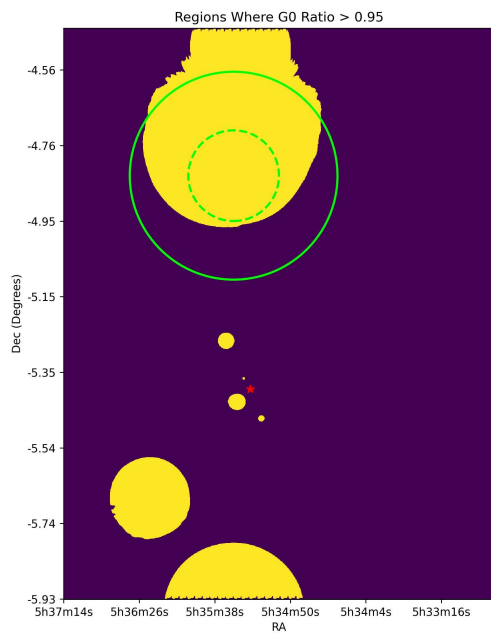


Figure B.1 The regions used for our average spectral analysis of NGC 1977. The inner, green, dashed circle defines our nearby region, while the annulus between the dashed and solid circles represents our outer region.

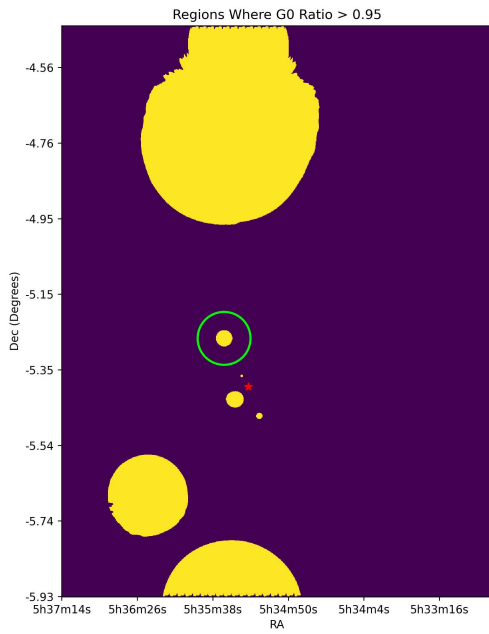


Figure B.2 The region (green circle) used in our average spectral analysis of M43.

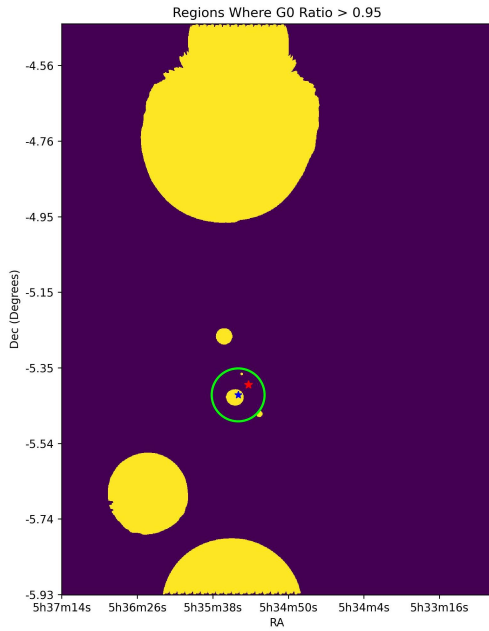


Figure B.3 The region (green circle) used in our average spectral analysis of the  $\theta^2$  Ori A area.

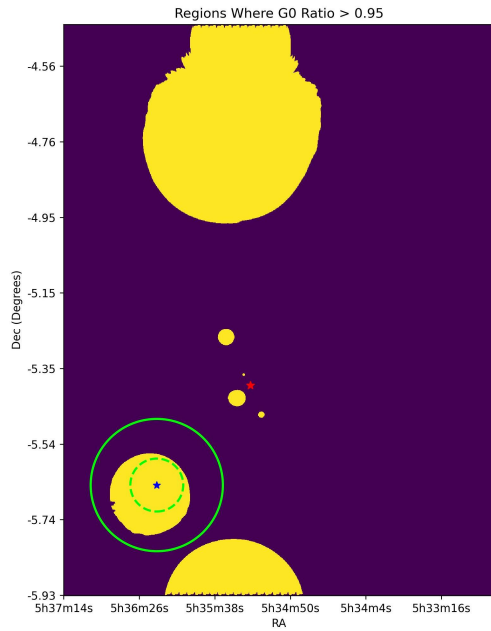


Figure B.4 The regions used for our average spectral analysis of the area around HD 37150. The inner, green, dashed circle defines our nearby region, while the annulus between the dashed and solid circles represents our outer region.

## B.2 PV Diagram Cut Regions

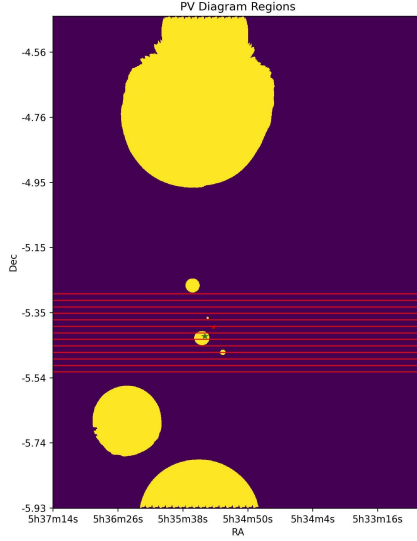


Figure B.5 The cuts used to create the PV diagrams in the  $\theta^2$  Ori A region (red lines). The height of each horizontal cut area is 70.5arcsec in declination. The location of  $\theta^2$  Ori A is marked in green.

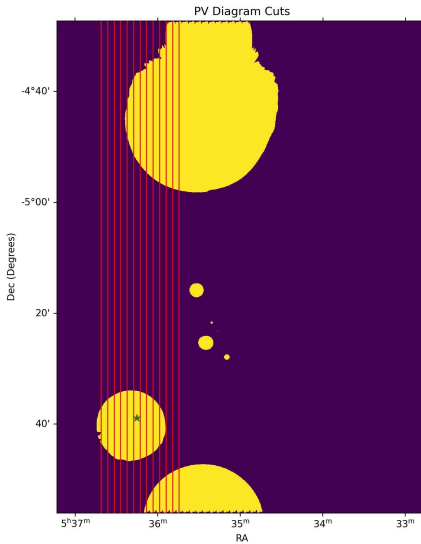


Figure B.6 The cuts used to create the PV diagrams in the HD 37150 region (red lines). The width of each vertical cut area is 70.5arcsec in right ascension. The location of HD 37150 is marked in green.

### B.3 HD 37150 Spectral Cross Regions

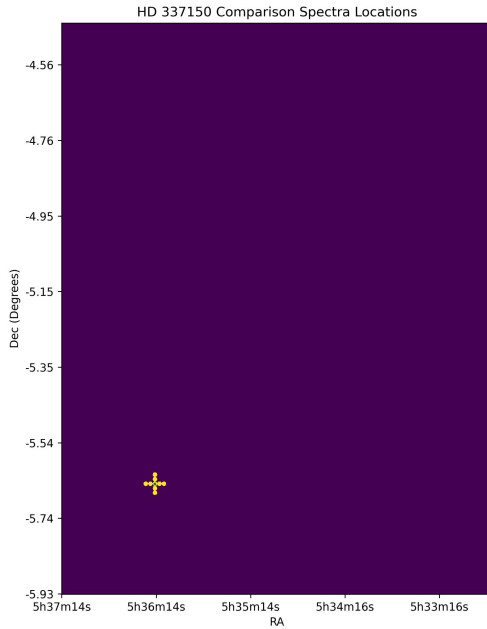


Figure B.7 The regions used for the 11 spectra in Figure 4.20. Each has a diameter of  $\sim 42$  arcsec, and the centers of each are offset by the same amount.